JACS
JOURNAL OF THE AMERICAN CHEMICAL SOCIETY
Article
pubs.acs.org/JACS

Structure–Activity Correlations in a Nickel–Borate Oxygen Evolution Catalyst

D. Kwabena Bediako,[†] Benedikt Lassalle-Kaiser,[‡] Yogesh Surendranath,[†] Junko Yano,[‡] Vittal K. Yachandra,*[,‡] and Daniel G. Nocera*[,†]

[†]Department of Chemistry, 6-335, Massachusetts Institute of Technology, Cambridge, Massachusetts 02139, United States
[‡]Physical Bioscience Division, Lawrence Berkeley National Laboratory, Berkeley, California 94720, United States

Supporting Information

ABSTRACT: An oxygen evolution catalyst that forms as a thin film from $Ni(aq)^{2+}$ solutions containing borate electrolyte ($Ni–B_i$) has been studied by in situ X-ray absorption spectroscopy. A dramatic increase in catalytic rate, induced by anodic activation of the electrodeposited films, is accompanied by structure and oxidation state changes. Coulometric measurements correlated with X-ray absorption near-edge structure spectra of the active catalyst show that the nickel centers in activated films possess an average oxidation state of +3.6, indicating that a substantial proportion of nickel centers exist in a formal oxidation state of Ni(IV). In contrast, nickel centers in nonactivated films exist predominantly as Ni(III). Extended X-ray absorption fine structure reveals that activated catalyst films comprise bis-oxo/hydroxo-bridged nickel centers organized into sheets of edge-sharing NiO_6 octahedra. Diminished long-range ordering in catalyst films is due to their ostensibly amorphous nature. Nonactivated films display a similar oxidic nature but exhibit a distortion in the local coordination geometry about nickel centers, characteristic of Jahn–Teller distorted Ni(III) centers. Our findings indicate that the increase in catalytic activity of films is accompanied by changes in oxidation state and structure that are reminiscent of those observed for conversion of β-NiOOH to γ-NiOOH and consequently challenge the long-held notion that the β-NiOOH phase is a more efficient oxygen-evolving catalyst.

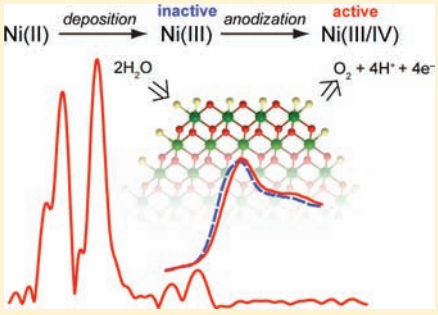

INTRODUCTION

Solar-driven water splitting to H_2 and O_2 is an attractive method of accomplishing the solar-to-fuels conversion necessary to meet the growing global energy demand by renewable sources.[1−5] Central to the efficiency of the overall photoelectrolysis process is the activity of the catalysts mediating the separate half-reactions that lead to H_2 and O_2 evolution. Of these two half-reactions, the oxygen evolution reaction (OER) is the more kinetically demanding,[6−15] imposing greater overpotential penalties that result in large losses to the overall efficiency of water splitting.[16] Accordingly, the widespread implementation of solar energy will benefit from the continued development of highly active oxygen evolution catalysts that efficiently couple multiple proton and electron transfers, accumulate the requisite four charge equivalents needed for water splitting over a narrow potential range, and collectively discharge these charge equivalents in O_2 formation.

Transition metal oxides are known to meet the requirements for highly active oxygen evolution catalysts,[17−19] with nickel oxides being the most attractive anode materials under alkaline conditions because of their low cost, high catalytic activity, and stability to corrosion.[19] Nickel oxyhydroxides and layered nickelates (NiOOX, where X = H or alkali metal ion) are also materials of choice as cathodes of alkaline batteries,[20] and this application more than any other has motivated numerous in situ structural and spectroscopic studies of these materials in concentrated alkali[21−24] and nonaqueous electrolytes.[25] Due to the technological imperative to suppress parasitic O_2 evolution during battery cathode charging, most previous studies have been directed toward determining the phases of NiOOH that are least proficient at catalyzing the OER. A general consensus has emerged that the β-NiOOH phase, with a formal nickel valency of ~3, is more active toward the OER than the more highly oxidized γ-NiOOH phase, with a formal Ni valency of ~3.6.[19,26] However, clear correlations of structure to OER activity are absent because the structure of the nickel oxide phase and its OER activity have not been simultaneously defined.

A challenge with constructing OER structure–function relationships for solid-state materials is to observe active sites relative to the bulk.[27−30] To this end, our recent discovery of heterogeneous catalyst films composed of molecular-like clusters[31−33] offers the opportunity to begin defining OER structure–function correlations because of a higher density of active-site species. We have shown that OER catalysts may be electrodeposited as thin films from solutions of $Co(aq)^{2+}$ and $Ni(aq)^{2+}$ and a proton-accepting electrolyte such as phosphate (P_i) or borate (B_i) (pH 7–9).[34−37] These catalysts mediate the OER under mild conditions and at high activity,[38] and accordingly they lend themselves to the construction of novel direct

Received: January 31, 2012
Published: March 14, 2012

   dx.doi.org/10.1021/ja301018q | J. Am. Chem. Soc. 2012, 134, 6801−6809

solar-to-fuels architectures such as the artificial leaf.[39−42] Nickel−borate (Ni−B_i) and cobalt−phosphate/borate (Co−P_i/Co−B_i) catalyst films may be self-assembled under nearly identical potential and pH conditions.[35,37] Yet the Ni−B_i films are unique because they require a subsequent oxidative pretreatment or anodization in order to attain a well-defined OER activity.[37] In contrast, maximal OER activity of Co−P_i/Co−B_i is observed immediately following electrodeposition and remains unchanged indefinitely.[43] The requirement for anodic pretreatment in the case of Ni−B_i leads us to postulate that an underlying structure and/or valency change was accompanying the marked increase in catalytic activity during the anodization process. This observation permits a structure−function correlation of OER activity to be undertaken with unprecedented fidelity. Because Ni−B_i is composed of small nanosized domains of NiOOH,[33] a much larger fraction of nickel centers are surface-exposed in Ni−B_i relative to its extended solid congeners, suggesting that its OER activity is far more sensitive to changes in average structure and nickel valency than extended NiOOH materials.

We now report in situ X-ray absorption spectroscopy (XAS) studies that track changes in nickel oxidation state and catalyst structure that accompany a greater than 2 orders of magnitude increase in OER activity during catalyst anodization. Correlation of coulometric measurements to in situ X-ray absorption near-edge structure (XANES) spectra reveal that anodization increases the average oxidation state of Ni−B_i films during catalysis, with fully activated films possessing a mean resting state nickel oxidation state of +3.6, in contrast to a mean resting state nickel oxidation state of about +3.16 for nonactivated films maintained at the same potential. On the basis of the structural parameters extracted from fitting extended X-ray absorption fine structure (EXAFS) data of anodized Ni−B_i films, we propose that the in situ catalyst attains a Ni(IV) oxidation state within sheets of edge-sharing NiO_6 octahedra with ordered domain sizes no smaller than 2 nm. The changes in oxidation state and short-range structure that accompany Ni−B_i anodization are evocative of the transformation of β-NiOOH to γ-NiOOH, challenging the long-held view[19,26] that the β-NiOOH phase effects more efficient OER catalysis.

EXPERIMENTAL SECTION

Catalyst Electrodeposition, Anodization, and Electrochemistry. Ni−B_i films were prepared on fluorine tin oxide (FTO) coated glass slides (Hartford Glass) by controlled potential electrolysis at 1.15 V (versus normal hydrogen electrode, NHE; all potentials hereafter are given versus NHE) of a quiescent 0.1 M potassium borate electrolyte, pH 9.2, (0.1-B_i) containing 0.40 mM Ni^{2+}. A total charge of 1.0 mC/cm^2 was passed during deposition. An Ag/AgCl reference electrode and Pt mesh counterelectrode were used for all electrochemical experiments. Following deposition, films were anodized in stirred 1.0 M KB_i electrolyte, pH 9.2 (1.0-B_i), by application of 1.1 V to catalyst films (with correction for ohmic potential losses) for 2.5 h. This preconditioning was also performed in 0.1-B_i on an independently deposited film. Nonanodized films were electrodeposited under identical conditions.

Cyclic voltammograms (CVs) were performed on electrodeposited films that were anodized in 1.0-B_i for times between 0 (nonanodized) and 4 h. The films were transferred immediately, without drying, to fresh 1.0-B_i. The electrode potential was maintained at 1.0 V for 30 s before the CV scan was performed from 1.0 V to lower potentials at a scan rate of 100 mV/s.

Film valency was determined coulometrically. Following electrodeposition and anodization, films were poised at 1.0 V for 300 s, after which the potential was immediately swept from 1.0 to 0.2 V and back to 1.2 V at 100 mV/s with compensation for ohmic potential losses. The cumulative charge passed during the scan was recorded; the amount of charge consumed in the reduction of nickel centers in the film was determined by subtracting the background charge passed by a 1 cm^2 FTO electrode (no catalyst coating) under identical conditions. Films were immediately removed from the electrolyte, allowed to dry in air, and subsequently dissolved in 5.00 mL of 2% aqueous nitric acid (Fluka Analytical, TraceSelect). Samples were analyzed for nickel content by quadrupole inductively coupled plasma mass spectrometry (ICP-MS; Elemental Analysis, Inc., Lexington, KY).

Model Ni Compounds. $NaNiO_2$ was prepared by annealing NiO and Na_2O_2 (Aldrich) in a flow of O_2 according to a previously published procedure.[44] γ-NiOOH was prepared by treating $NaNiO_2$ with 5 mol equiv of Br_2 in acetonitrile.[44] β-NiOOH was prepared by treating a suspension of $Ni(OH)_2$ in 3 M aqueous KOH with 0.7 mol equiv of Br_2. The identity and purity of each compound were verified by powder X-ray diffraction (XRD). $Ni(OH)_2$, Br_2, and $K_2Ni(H_2IO_6)_2$ were purchased from Aldrich.

Catalyst Preparation for in Situ X-ray Absorption Spectroscopy. A glass electrochemical cell consisting of two compartments separated by a porous frit was employed for in situ spectroscopic experiments, The working compartment possessed flat walls (∼2.5 cm wide) with a single circular hole, 1.5 cm in diameter. A 3 cm × 2 cm slip of ITO-coated poly(ethylene terephthalate) (Kintec Company) was affixed with epoxy glue to the exterior of the wall of the cell, over the 1.5-cm hole, with the ITO layer (∼0.15 μm thick) facing inward. This ITO surface served as the substrate for electrodeposition of Ni−B_i films. The cell was connected to the potentiostat by making electrical contact to a portion of the ITO slip that protruded from the side of the working compartment. A Teflon cap containing a hole for the reference electrode was used to cover the working compartment and to ensure a fixed distance between working and reference electrodes between experiments.

Catalyst electrodeposition for XAS experiments was terminated after 1.0 mC/cm^2 was passed. The cell was emptied of electrolyte and rinsed twice with water (18 MΩ resistivity, EMD Millipore). For anodized films, the electrochemical cell was charged with 1.0-B_i, and anodization was carried out at 1.3 V with stirring and without compensation for ohmic potential losses over a period of 3 h, after which spectra were collected over a range of applied potentials between 1.0 and 1.15 V. For nonanodized films, the electrochemical cell was refilled with 0.1-B_i after deposition and spectra were acquired at 1.0 V.

X-ray Absorption Spectroscopy Data Collection and Analysis. XAS spectra were collected at the Stanford Synchrotron Radiation Lightsource (SSRL) on beamline 7-3 at an electron energy of 3.0 GeV with an average current of 300 mA and at the Advanced Light Source (ALS) on beamline 10.3.2 at an electron energy of 1.9 GeV with an average current of 500 mA. At beamline 7-3 (SSRL), the radiation was monochromatized by a Si(220) double-crystal monochromator. The intensity of the incident X-ray was monitored by an N_2-filled ion chamber (I_0) in front of the sample. Model compound solid samples were diluted in boron nitride (1% w/w) and placed in an aluminum sample holder sealed with kapton tape. Data were collected as fluorescence excitation spectra with a Ge 30 element detector (Canberra). For model compounds, energy was calibrated by the first peak maximum of the first derivative of a nickel foil (8333.0 eV). The standard was placed between two N_2-filled ionization chambers (I_1 and I_2) after the sample. At beamline 10.3.2 (ALS), the radiation was monochromatized by a Si(111) double-crystal monochromator. Intensity of the incident X-ray was monitored by an N_2-filled ion chamber (I_0) in front of the sample. Fluorescence spectra were recorded by using a seven-element Ge detector array (Canberra). For electrochemical experiments, no transmission data could be collected. The energy was therefore calibrated by use of a glitch in the I_0 intensity. All data were collected at room temperature.

Data reduction of the EXAFS spectra was performed by use of EXAFSPAK (Drs. Graham George and Ingrid Pickering, SSRL). Pre- and post-edge backgrounds were subtracted from the XAS spectra, and the results were normalized with respect to edge height. Background removal in k-space was achieved through a five-domain cubic spline.

dx.doi.org/10.1021/ja301018q | J. Am. Chem. Soc. 2012, 134, 6801−6809

Curve fitting was performed with Artemis and IFEFFIT software using ab initio-calculated phases and amplitudes from the program FEFF 8.2.[45,46] These ab initio phases and amplitudes were used in the EXAFS equation:

$$\chi(k) = S_0^2 \sum_j \frac{N_j}{kR_j^2} f_{\mathrm{eff}_j}(\pi, k, R_j)\, e^{-2\sigma_j^2 k^2} e^{-2R_j/\lambda_j(k)} \times \sin[2kR_j + \phi_{ij}(k)] \quad (1)$$

The neighboring atoms to the central atom(s) are divided into j shells, with all atoms with the same atomic number and distance from the central atom grouped into a single shell. Within each shell, the coordination number N_j denotes the number of neighboring atoms in shell j at a distance of R_j from the central atom. $f_{\mathrm{eff}}(\pi, k, R_j)$ is the ab initio amplitude function for shell j, and the Debye–Waller term $e^{-2\sigma_j^2 k^2}$ accounts for damping due to static and thermal disorder in absorber–backscatterer distances. The mean free path term $e^{-2R_j/\lambda_j(k)}$ reflects losses due to inelastic scattering, where $\lambda_j(k)$ is the electron mean free path. The oscillations in the EXAFS spectrum are reflected in the sinusoidal term $\sin[2kR_j + \varphi_{ij}(k)]$, where $\varphi_{ij}(k)$ is the ab initio phase function for shell j. S_0^2 is an amplitude reduction factor due to shakeup/shake-off processes at the central atom(s). The EXAFS equation was used to fit the experimental data with N, R, and the EXAFS Debye–Waller factor (σ^2) as variable parameters. For the energy (electronvolts) to wave vector (k, angstrom^{-1}) axis conversion, E_0 was defined as 8340 eV, and the S_0^2 value was fixed to 0.83.[25] EXAFS curve-fitting procedures and the estimation of the uncertainty in the parameters from the fits are described in detail in the Supporting Information.

RESULTS

Catalyst Electrodeposition, Anodization and Electrochemistry. Catalyst films were prepared by controlled potential electrolysis of 0.1 M KB_i, pH 9.2, electrolyte (0.1-B_i) containing 0.40 mM $Ni(aq)^{2+}$. In our initial communication,[37] we reported that catalyst films were prepared by subjecting stirred 1 mM $Ni(aq)^{2+}$ solutions in 0.1-B_i to bulk electrolysis at 1.3 V with the passage of 0.3–10 C/cm^2. Similarly, the ex situ XAS study of Ni–B_i[33] followed the same basic procedure to prepare the catalyst. Whereas catalyst films deposit rapidly under these conditions, such films suffer from poor adhesion to the substrate and heterogeneity in thickness over the electrode surface, in part due to the nonuniform rate of mass transport to different parts of the electrode under these conditions. For the purpose of the studies reported here, much thinner and more uniform films were desired. Films were prepared therefore from less concentrated $Ni(aq)^{2+}$ solutions and at an applied potential of 1.15 V without stirring. The passage of 1.0 mC/cm^2 during deposition required a period of 60–80 s. Because oxygen evolution is coincident with film formation at these potentials, the charge passed is not expected to be strictly representative of the number of nickel centers in the film. But this value does allow for an initial upper-limit estimate of catalyst loading for these brief deposition times. Such films therefore contain <10 nmol/cm^2 and are <7 nm thick (see Supporting Information). Following electrodeposition, films were anodized in stirred 1.0 M KB_i, pH 9.2, electrolyte (1.0-B_i) by application of 1.1 V (with correction for ohmic potential losses) for 2.5 h. Over the course of anodization, the current density increased by more than 2 orders of magnitude (Figure 1). Alternatively, films could be anodized by passing 3.5 mA/cm^2 over a similar duration, resulting in a decrease of about 300 mV in measured potential (Figure S1, Supporting Information). Operation of the catalyst at 1.1 V in 0.1-B_i, with compensation for ohmic losses, results in a very gradual increase in the current density over time (Figure S2, Supporting Information), with no plateau in activity observed after 3 h. These results demonstrate that the rate of anodization is dependent on electrolyte concentration.

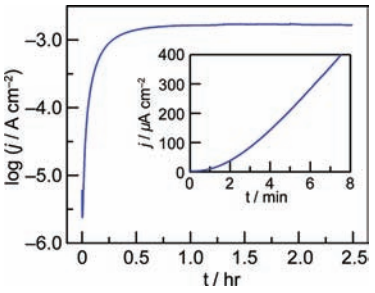

Figure 1. Change in oxygen evolution current density as a function of anodization duration for a 1 mC/cm^2 Ni–B_i catalyst film on an FTO substrate, operated at 1.1 V (versus NHE) for 2.5 h in Ni-free 1.0 M KB_i electrolyte, pH 9.2. (Inset) Magnification of the first 8 min of the anodization process on a linear current density scale.

Figure 2 displays the cyclic voltammograms (CVs) for independently prepared films (1.0 mC/cm^2) subject to anodization for varying times. For freshly deposited nonanodized films, the initial sweep from 1.0 V to more negative potentials results in a broad and asymmetric cathodic wave with a shoulder at 0.87 V and a peak at $E_{p,c}$ = 0.81 V, corresponding to reduction of the surface-adsorbed species. The return scan to more positive potentials displays an anodically shifted oxidation wave centered at $E_{p,c}$ = 1.05 V; onset of a catalytic wave is not observed until ~1.13 V. With anodization, the cathodic and anodic waves of the surface-adsorbed species become sharper and more symmetric, and the catalytic wave shifts to lower potential and becomes more pronounced. There is no difference in the voltammetric features of films anodized after 2 h; both 2 h- and 4 h-anodized films display cathodic and anodic waves centered at $E_{p,c}$ = 0.87 V and $E_{p,a}$= 1.025 V, respectively. The inset of Figure 2 shows the ratio of the charge passed in the reductive sweep for films at different times of anodization (Q) to that of the 4-h anodized film (Q_{final}).

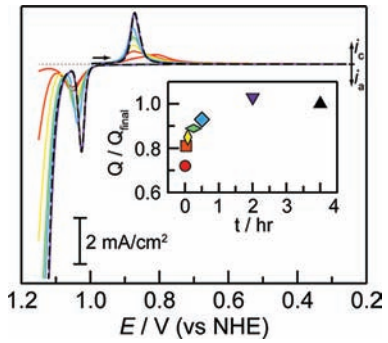

Figure 2. Cyclic voltammograms (CVs) in 1.0 M KB_i (pH 9.2) electrolyte at 100 mV/s of 1 mC/cm^2 Ni–B_i catalyst films, nonanodized (red) and after 2 min (orange), 5 min (yellow), 15 min (green), 30 min (light blue), 2 h (blue), and 4 h (black) of anodization at 1.1 V (vs NHE) in 1.0 M KB_i (pH 9.2) electrolyte. The background CV of a blank FTO substrate is also displayed (gray). (Inset) Ratio of integrated charge under the cathodic wave observed in the first scan to lower potentials in the case of each film relative to that of the 4 h-anodized film.

dx.doi.org/10.1021/ja301018q | J. Am. Chem. Soc. 2012, 134, 6801–6809

Quantitative determination of the average oxidation state of nickel in anodized Ni−B_i catalyst films at 1.0 V was obtained by determining the charge required to discharge such films to the reduced Ni(II) state. Following anodization, films were held at 1.0 V for 300 s to allow the current density to attain a steady-state value (~1 μA/cm^2). At 300 s, the potential was swept at 100 mV/s without pause to 0.2 V and back to 1.2 V. A background subtraction was employed to eliminate any excess charge caused by miscellaneous faradaic processes occurring at the FTO substrate alone. Such charges accounted for less than 2% of the total charge passed. Determination of the cumulative charge passed during each sweep segment (Figure S3, Supporting Information) permits calculation of the mean number of electrons consumed per nickel center, provided the amount of nickel on the electrode can be accurately determined. Catalyst loading was quantified by digestion of films in a known volume of dilute acid immediately after the electrochemical experiment. CVs of the FTO substrates in 1.0-B_i electrolyte after film dissolution were indistinguishable from background CVs collected before electrodeposition, indicating that dissolution was quantitative. Digests were analyzed for nickel concentration by ICP-MS. The results of such measurements on three independent films and the computed number of electrons discharged per nickel center (about 1.6 in each case) are listed in Table 1. These coulometric experiments establish an average nickel oxidation state of +3.61(7) for anodized Ni−B_i films biased at 1.0 V.

Table 1. Coulometric Titration of Ni−B_i Catalyst Films

charge[a] (mC)	Ni loading[b] (nmol)	no. of e$^-$ consumed per Ni
1.14	7.5 (0.2)	1.63 (0.04)
1.13	7.2 (0.2)	1.62 (0.04)
1.08	7.1 (0.2)	1.58 (0.04)

[a]Total charge passed upon reduction of anodized Ni−B_i catalyst films at 0.2 V. [b]Determined by quadrupole ICP-MS.

This coulometric measurement also allows us to determine the average oxidation state of nickel centers in nonanodized films. As shown in the inset of Figure 2, the electrochemical reduction of nonanodized films to their Ni(II) state consumes 72% of the charge required to reduce anodized films. This implies an average number of electrons discharged per nickel center of about 1.16 and defines an average oxidation state of +3.16(5) for films prior to anodization.

In Situ X-ray Absorption Spectroscopy. Nickel K-edge X-ray absorption spectra (XAS) were collected on Ni−B_i films deposited on an ITO electrode. The precise deposition sequence for the nonanodized and anodized films is described in the Experimental Section. In both cases, XAS spectra were collected 5 min after applying a potential to ensure that the system had reached steady-state.

Figure 3a presents the XANES spectra of an anodized Ni−B_i film poised at 1.0 and 0.4 V, together with model compounds $Ni(OH)_2$, β-NiOOH, γ-NiOOH, and $K_2Ni(H_2IO_6)_2$ [potassium nickel(IV) paraperiodate, NiPPI]) possessing formal nickel oxidation states of +2, +3, +3.6, and +4, respectively. The edge position of each model compound shifts to higher energies with increasing formal oxidation state. The edge position of the crystalline γ-NiOOH compound used in this study, which is an off-stoichiometric compound with a formal nickel oxidation state of about +3.6,[44] is approximately halfway (8345.0 eV, measured at half height F/I_0 = 0.5) between the stoichiometric

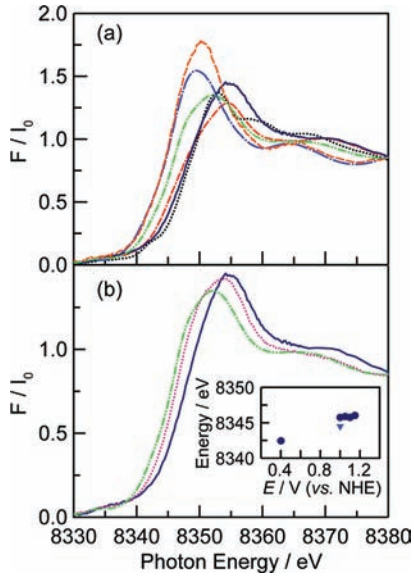

Figure 3. (a) XANES spectra of model compounds: $Ni(OH)_2$ (blue broken line), β-NiOOH (green broken line), γ-NiOOH (red broken line), NiPPI (black dotted line), and anodized Ni−B_i films at 0.4 (orange dashed line) and 1.0 V (dark blue solid line). (b) XANES spectra of a nonanodized Ni−B_i film poised at 1.0 V (purple dotted line), an anodized Ni−B_i film poised at 1.0 V (dark blue solid line), and β-NiOOH (green broken line). (Inset) Edge energy at half jump height as a function of applied potential for anodized (dark blue circles) and nonanodized (blue triangle) Ni−B_i.

Ni(III) compound β-NiOOH (8343.7 eV) and stoichiometric Ni(IV) compound NiPPI (8346.4 eV). The edge shape and position of the anodized film in its fully oxidized state (poised at 1.0 V) (8345.8 eV) is similar to that of γ-NiOOH (8345.0 eV), whereas in its fully reduced state (poised at 0.4 V), the edge shape and position of the anodized film (8342.5 eV) matches that of $Ni(OH)_2$ (8342.4 eV), indicating a mean oxidation state of +2. Although the edge position of a XANES spectrum is not a straightforward indicator of the oxidation state of metals owing to the several parameters that contribute to the XANES spectra (i.e., charge density, ligand symmetry, and spin density),[47] the trend observed here indicates that anodized Ni−B_i films poised at 1.0 V possess significant Ni(IV) content, with a mean oxidation state of nickel centers near +3.6, consistent with the coulometric measurements. For anodized Ni−B_i films poised at potentials of 1.15, 1.10, 1.05, and 1.00 V (Figure 3b inset), there was essentially no shift in the XANES edge energy. We therefore surmise that over this potential range anodized Ni−B_i films do not display any changes in average nickel oxidation state despite the 3 orders of magnitude change[37] in the rate of catalytic turnover.

XANES spectra were also collected on a nonanodized Ni−B_i film under 1.0 V applied potential in 0.1-B_i. Because anodization is not pronounced under these conditions (Figure S2, Supporting Information), XAS spectra of such films are expected to be mostly representative of films prior to anodization with low catalytic activity. As shown in Figure 3b, the XANES spectrum of a nonanodized Ni−B_i film poised at 1.0 V displays an edge energy of 8344.5 eV (at F/I_0 = 0.5), which lies 0.8 eV positive of that of the stoichiometric Ni(III) compound β-NiOOH (8343.7 eV) and 1.3 eV below the edge position of anodized films held at the same potential (8345.8 eV). This edge position suggests a formal nickel oxidation state for the nonanodized films between +3 and +3.6.

dx.doi.org/10.1021/ja301018q | J. Am. Chem. Soc. 2012, 134, 6801−6809

EXAFS data were collected on anodized Ni−B_i films poised at 1.05 and 1.15 V. The spectra of the anodized catalyst films at the two potentials displayed marginal differences, with slightly higher overall EXAFS intensities observed when the film is polarized at higher potential (Figure S4, Supporting Information). The EXAFS spectrum of anodized Ni−B_i is comparable to the EXAFS spectrum of γ-NiOOH. The crystal structure[44,48] of γ-NiOOH is shown in Figure 4a, and a fragment of the edge-sharing

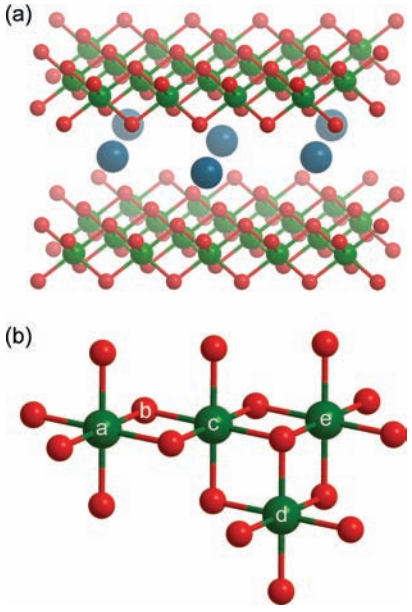

Figure 4. (a) X-ray crystal structure of γ-NiOOH, showing nickel (green), oxygen (red), and sodium (blue) ions. Water molecules intercalated between the NiO_2 slabs have been omitted for clarity. (b) Fragment of a general nickelate structure displaying the atoms (b−e) that lead to the relevant backscattering interactions from the absorbing atom, a.

NiO_6 octahedra that comprise the layered material is presented in Figure 4b. Figure 5 presents the k^3-weighted EXAFS spectra and the corresponding Fourier transform (FT) recorded for an anodized catalyst film maintained at 1.05 V, together with that of γ-NiOOH. The abscissa in the FT spectra is the apparent distance (R'), which is shorter than the actual distance between the absorber−backscatterer atom pairs due to a phase shift. The EXAFS spectra display two main peaks: peak I reflects the presence of Ni−O interactions (path a−b in Figure 4b), and peak II manifests Ni−Ni interactions (path a−c), as demonstrated by the EXAFS fits (vide infra). The positions of peaks in the FT EXAFS spectra of anodized Ni−B_i films are similar to those of γ-NiOOH but there are differences in peak intensity. In particular, peak IV, corresponding to longer-range interactions (path a−e) is suppressed significantly in the FT EXAFS spectrum of the catalyst film as compared to what is found in the case of the crystalline γ-NiOOH. When an anodized catalyst film is reduced to Ni(II) by maintaining the potential at 0.4 V, the EXAFS spectrum becomes similar to that of $Ni(OH)_2$ (Figure S5, Supporting Information) with longer Ni−O and Ni−Ni distances.

The EXAFS curve fitting was first carried out for γ-NiOOH based on its known crystal structure, by including absorber−backscatterer vectors ≤5.8 Å in length and fixing the number of neighbors in each shell (N values) to values determined from the crystal structure (6.0 in each case).[44,48] Figure 6 shows the k-space and FT spectra of the best fit, and Table 2 summarizes

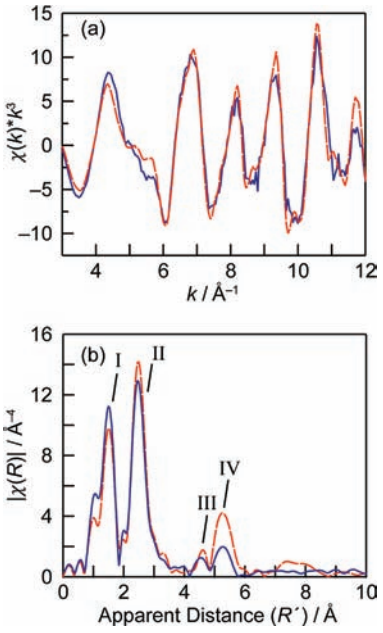

Figure 5. EXAFS spectra and Fourier transforms for γ-NiOOH (red dashed lines) and anodized Ni−B_i during catalysis at 1.05 V (blue solid lines). (a) k^3-weighted EXAFS oscillations. (b) Fourier transforms of k-space oscillations.

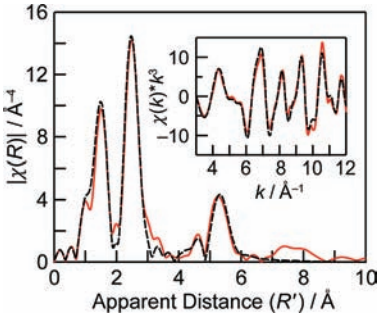

Figure 6. Fit (black dashed lines) to EXAFS spectrum of γ-NiOOH (red solid lines). (Inset) Corresponding k^3-weighted oscillations. Fit parameters are indicated in Table 2.

Table 2. γ-NiOOH EXAFS Fitting Parameters[a]

	R (Å)					
path	XRD	EXAFS	N^b	σ^2 (Å^{-2})	ΔE^0 (eV)	R_f (%)
Ni−O	1.90	1.88 (0.01)	6.0	0.007 (0.001)	2.3	3.4
Ni−Ni	2.83	2.82 (0.01)	6.0	0.006 (0.001)		
Ni−Ni	4.90	4.88 (0.04)	6.0	0.012 (0.005)		
Ni−Ni[c]	5.66	5.70 (0.01)	6.0	0.004 (0.001)		

[a]Fitting region $1 \le R \le 6$, $2.9 \le k \le 11.9$. Values in parentheses indicate uncertainties. See Supporting Information for details. [b]Fixed values. [c]Multiple scattering path (a−e; Ni−Ni−Ni)

the fitting parameters. The actual distances (R) of the EXAFS fits are in good correspondence with the crystallographic distances of γ-NiOOH. With these results in hand for the model compound, the fit of the experimental spectrum of anodized Ni−B_i was produced (Figure 7). In order to estimate a lower-limit domain size, the Debye−Waller factors (σ^2) were fixed to the values obtained from γ-NiOOH EXAFS curve fitting (Table 2),

dx.doi.org/10.1021/ja301018q | J. Am. Chem. Soc. 2012, 134, 6801−6809

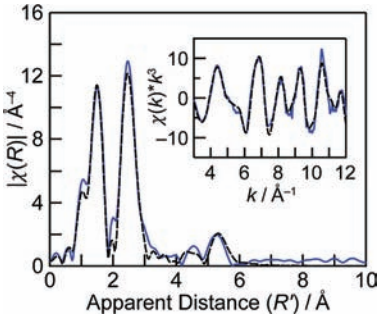

Figure 7. Fit (black dashed lines) to EXAFS spectrum of anodized Ni−B_i at 1.05 V (blue solid lines). (Inset) Corresponding k^3-weighted oscillations. Fit parameters are indicated in Table 3.

and the N values were optimized for the best fit. We consider these σ^2 values to be a reasonable lower limit because static disorder is expected to be lower in the crystalline γ-NiOOH compound relative to Ni−B_i. The resulting fit, which is displayed in Figure 7 with fitting parameters in Table 3, returns an

Table 3. Anodized Ni−B_i Catalyst EXAFS Fitting Parameters[a]

path	R (Å)	N	σ^2 [b] (Å^{-2})	ΔE^0 (eV)	R_f (%)
Ni−O	1.89 (0.01)	5.9 (0.4)	0.007	3.3	3.1
Ni−Ni	2.82 (0.01)	5.1 (0.3)	0.006		
Ni−Ni	4.86 (0.07)	4.1 (3.2)	0.012		
Ni−Ni[c]	5.70 (0.03)	2.7 (1.1)	0.004		

[a]Fitting region $1 \le R \le 6$, $2.8 \le k \le 11.8$. Values in parentheses indicate uncertainties. See Supporting Information for details. [b]The σ^2 values were set to the values obtained from γ-NiOOH curve fitting. [c]Multiple scattering path (a−e; Ni−Ni−Ni).

N value for the Ni−Ni vector (with R = 2.82 Å) of ∼5. Much weaker peaks arising from interactions at distances >3 Å (peaks III and IV) also suggests a less-ordered structure or smaller cluster size in the Ni−B_i film compared to the crystalline γ-NiOOH compound. A *lower-limit* domain size consisting of ∼40 Ni ions for the seemingly amorphous catalyst film is estimated from this Ni−Ni N value.

EXAFS data were collected on a nonanodized Ni−B_i film poised at 1.0 V to provide insight into the local structure of the catalyst film in its initially deposited, less catalytically active state. β-NiOOH was considered a preliminary model compound for such films, since it displayed the closest mean Ni oxidation state (Figures 2 and 3b). Figure 8 compares the

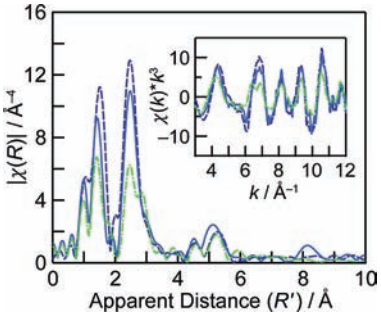

Figure 8. EXAFS FT spectra for nonanodized Ni−B_i poised at 1.0 V (blue solid lines), anodized Ni−B_i poised at 1.05 V (dark blue dashed lines), and β-NiOOH (green broken lines). (Inset) Corresponding k^3-weighted oscillations.

EXAFS spectrum of a nonanodized Ni−B_i film to that of its anodized congener and β-NiOOH. The EXAFS FT of a nonanodized Ni−B_i film presents peaks at distances similar to those of anodized films, yet with much lower intensities (Figure 8). The peak intensities for β-NiOOH are lower than those of either Ni−B_i film. For both $NaNiO_2$ and β-NiOOH, the best fits (Tables S1 and S2, Supporting Information) were obtained by considering two distinct sets of distances for the first- and second-shell vectors that reflect a Jahn−Teller distortion (Figure S7, Supporting Information).[49,50] With β-NiOOH, the best fit to the EXAFS spectrum yields a ratio of long and short Ni−O interaction numbers of 3.9:2.1, which is similar to the 4:2 ratio expected from the Jahn−Teller distortion. An excellent fit was obtained for the nonanodized film (Figure 9) with a ratio of

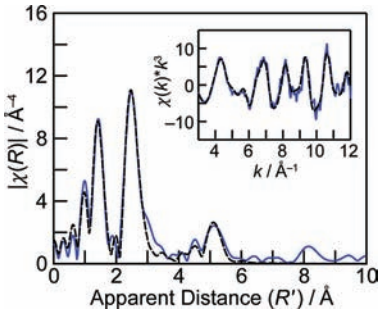

Figure 9. Fit (black dashed lines) to EXAFS spectrum of nonanodized Ni−B_i poised at 1.0 V (blue solid lines). (Inset) Corresponding k^3-weighted oscillations. Fit parameters are indicated in Table 4.

long to short Jahn−Teller distorted vectors of about 4:2 (Table 4). Importantly, the fit quality suffers appreciably (R_f = 7.1% versus

Table 4. As-Deposited Ni−B_i Film EXAFS Fitting Parameters[a]

path	R (Å)	N[b]	σ^2 [c] (Å^{-2})	ΔE^0 (eV)	R_f (%)
Ni−O	1.90 (0.01)	4.0 (0.4)	0.003 (0.001)	5.7	2.0
Ni−O	2.10 (0.03)	2.0 (0.4)	0.003 (0.001)		
Ni−Ni	2.83 (0.01)	4.6 (0.3)	0.005 (0.001)		
Ni−Ni	3.05 (0.03)	1.4 (0.3)	0.005 (0.001)		

[a]Fitting region $1.0 \le R \le 3.6$, $2.55 \le k \le 12.52$. Values in parentheses indicate uncertainties (see Supporting Information). [b]Sum of the N values for the short and long interactions was fixed to 6. [c]σ^2 values were set to be equal for the short and long interactions.

2.0%) when only a single path is considered for the first- and second-shell vectors (Table S3, Supporting Information). These fitting results point to a distortion in the local coordination geometry about Ni centers in nonanodized Ni−B_i films, as found in β-NiOOH and $NaNiO_2$.

■ DISCUSSION

A Ni−B_i catalyst film requires a pre-electrolysis regimen following electrodeposition to obtain high OER activities. Over the course of this anodization, the efficiency of Ni−B_i films in mediating the OER is enhanced by greater than 2 orders of magnitude, as indicated by Figure 1. This drastic improvement in catalytic activity is reflected in the prominence of the catalytic wave in CVs of anodized films compared to the diminished catalytic wave at identical potentials in those of

dx.doi.org/10.1021/ja301018q | J. Am. Chem. Soc. 2012, 134, 6801−6809

nonanodized films (Figure 2). Narrower and more symmetric voltammetric peak shapes for CVs of anodized catalyst films indicate that the anodization process results in greater homogeneity in the nickel oxidation potential. The rate of anodization is sensitive to the electrolyte concentration (Figure 1 versus Figure S2, Supporting Information). By using low electrolyte concentrations, we have been able to retard anodization to the extent that over the time course of XAS data collection, we are able to monitor, in situ, the structural and oxidation-state changes that accompany anodization and the attendant increase in catalytic activity.

Nickel Oxidation State Changes in Ni−B_i. Coulometric and XANES studies corroborate the average oxidation state of nickel in Ni−B_i for anodized and nonanodized films subjected to various potentials. For both anodized and nonanodized films, polarization at potentials well below the onset potential for water oxidation catalysis (0.4 V) induces complete reduction of the nickel centers to the +2 oxidation state (Figure 2). Conversely, anodized films polarized at 1.0 V, a potential at which oxygen evolution catalysis occurs, exhibit a mean oxidation state of +3.6 (Figures 2 and 3a, Table 1), whereas nonanodized films, held at the same potential, exhibit a mean oxidation state of +3.16 (Figures 2 and 3b). Thus the process of anodization increases the fraction of Ni(IV) centers in the film by at least a factor of 3 (from 20% to 60%) over the course of 4 h (Figure 2). Coulometric studies establish that the vast majority of this oxidation state change occurs within the first hour of anodization (Figure 2). This time window corresponds qualitatively to the time scale over which the vast majority of increase in OER activity is observed (Figure 1). The similar time course observed for activity and oxidation state increases points to a strong correlation between the two properties.

The increase in nickel oxidation state from +3.16 to +3.6 is concordant with the oxidation state change observed for phase conversion of β-NiOOH to γ-NiOOH. Importantly, polarization of the anodized Ni−B_i films beyond 1.0 V, up to a potential of 1.15 V, does not engender any further increase in the average formal oxidation state of nickel centers (Figure 3b inset), despite the fact that this same increase in potential corresponds to a 3 orders of magnitude increase in the rate of OER catalysis.[37] Together, these results establish that an increase in the Ni(IV) population in the catalyst resting state is correlated with an increase in overall activity. Moreover, because there is no detectable change in the XANES edge shift of anodized films (Figure 3b inset) between 1.0 and 1.15 V, the mechanism of action of catalytically active sites in the anodized film likely involves a further minor equilibrium, possibly from Ni(III) resting states to Ni(IV) catalytic intermediates.

Anodization-Induced Structural Changes in Ni−B_i. The similarities between crystalline γ-NiOOH and anodized Ni−B_i catalyst films in terms of XANES edge position, formal nickel oxidation state, and EXAFS spectra indicate that γ-NiOOH is an appropriate model compound for the structure of anodized Ni−B_i catalyst films. In γ-NiOOH, edge-sharing NiO_6 octahedra are arranged into higher-order layers, which are interstratified with alkali cations and water molecules (Figure 4). EXAFS spectra of anodized Ni−B_i catalyst films exhibit a first-shell Ni−O vector at 1.89 Å and a nearest-neighbor Ni−Ni vector at 2.82 Å associated with the presence of Ni-oxo/hydroxo structural units similar to those found in γ-NiOOH (Figure 5). The γ-NiOOH structure is differentiated from β-NiOOH (and $NaNiO_2$) by a Jahn−Teller distortion of the low-spin d^7 Ni(III) centers of the latter, which gives rise to an axial elongation and equatorial contraction of the oxygen ion ligand field, producing a 2:1 ratio of Ni−O scattering vectors of 1.87 and 2.03 Å, respectively (Figure S7, Supporting Information).[50] This Jahn−Teller distortion in β-NiOOH results in two effects that distinguish its EXAFS spectrum from γ-NiOOH (and anodized Ni−B_i): (i) a drastic diminution in the intensity and (ii) broadening of the first- and second-shell scattering peaks arising from their poorly resolved splitting into two separate sets of peaks corresponding to a ∼4:2 ratio of short equatorial and long axial vectors, respectively, about each Ni(III) center. The sharp peaks observed for first and second shell of Ni−Ni and Ni−O scattering vectors in the experimental spectrum of anodized Ni−B_i are similar to the peak profiles of γ-NiOOH, and thus the local coordination geometry of anodized Ni−B_i is akin to γ-NiOOH and not a Jahn−Teller distorted Ni(III) phase, such as β-NiOOH or $NaNiO_2$.

Whereas anodized Ni−B_i is structurally analogous to γ-NiOOH, nonanodized Ni−B_i has an EXAFS spectrum that is more similar to a Jahn−Teller distorted Ni(III) phase. A good fit to the nonanodized Ni−B_i spectrum (Figure 9) is obtained with a long to short axis ratio of 4.0 to 2.0 for the Ni−O vectors (Table 4), the ratio we expect for a Ni(III) compound. A slightly greater formal nickel oxidation state (+3.16) was determined from coulometric measurements, and correspondingly the XANES edge position is 0.8 eV higher relative to that of β-NiOOH (Figure 3b). These EXAFS results point to a local structural change upon anodization of Ni−B_i that resembles phase conversion of β-NiOOH to γ-NiOOH.

While the nickelate layers of β-NiOOH and γ-NiOOH stack preferentially, we were unable to identify any interactions due to interlayer backscattering in either model compound or catalyst film. However, given the large intersheet distance (∼7 Å) in γ-NiOOH,[44] such interactions are expected to be too weak to resolve in EXAFS spectra and would be anticipated to be even weaker in the case of the more disordered catalyst material. Despite the inability to detect any interlayer scattering interactions by EXAFS, some degree of stacking of the sheetlike domains of Ni−B_i is evident. The electrolyte concentration dependence of the rate of anodization (Figure S2, Supporting Information) provides experimental evidence in support of this contention. Cation intercalation is a critical requirement for the formation of γ-NiOOH from the alkali cation-free β-NiOOH.[51] The intercalation of K^+ ions between the NiO_2 sheets in Ni−B_i films during anodization may explain the observed electrolyte dependence. Thus increasing the buffer strength, and correspondingly the K^+ ion activity, would be expected to enhance the rate of activation, provided that the domains of Ni−B_i are stacked to some degree.

The size of the ordered domains in anodized Ni−B_i may be estimated from the N values obtained from curve fitting (Figure 7) of EXAFS spectra. The diminished longer-range interactions (at distances >3 Å) in FT EXAFS spectra, compared to an extended solid (Figure 5b, red dashed lines versus blue solid lines), suggest a nanocrystallite model, as does the inability to detect crystallites by X-ray diffraction methods. From the N-value for the Ni−Ni vector of ∼5.1 (Table 3), we estimate that the smallest ordered domains in catalyst films are 2−3 nm in diameter. Thus, a simplified hexagonal cluster model is constructed with ordered domains of ∼40 Ni centers (Figure 10) as a reasonable lower-limit average structural model for Ni−B_i catalyst films. We therefore rationalize that our Ni−B_i electrosynthesis method is giving us access to such nanocrystalline oxides as uniform ultrathin films at intermediate pH.

dx.doi.org/10.1021/ja301018q | J. Am. Chem. Soc. 2012, 134, 6801−6809

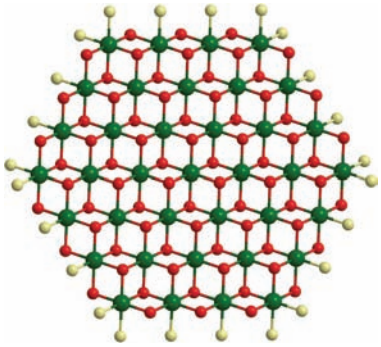

Figure 10. Lower-limit structural model for the average domain size of Ni−B_i. Ni ions are shown in green, bridging oxo/hydroxo ligands are shown in red, and nonbridging oxygen ligands, which may include water, hydroxide, or borate, are shown in pale green.

CONCLUSION

Anodization of electrodeposited films, which results in an almost 3 orders of magnitude improvement in catalyst activity, is accompanied by an increase in average nickel oxidation state to Ni(IV) and alteration of the structure of the nickel centers in electrodeposited ultrathin Ni−B_i catalyst films. A significant positive shift in the XANES edge to a position indicative of substantial formal Ni(IV) valency is observed, and EXAFS spectra indicate the presence of μ-oxo/hydroxo nickel centers organized into higher-order domains of edge sharing NiO_6 octahedra. As-deposited, Ni−B_i films display evidence for a Jahn−Teller distorted coordination geometry about the predominantly Ni(III) centers, reminiscent of the short-range structure of β-NiOOH. In contrast, anodized films possess short-range structural parameters akin to the mixed-valent γ-NiOOH phase. Thus, XAS spectra reveal that the short-range structure of anodized Ni−B_i is similar to γ-NiOOH, and that of nonanodized Ni−B_i is similar to β-NiOOH. Electrochemical, XANES, and EXAFS data point to a conversion of local structure and nickel oxidation state in Ni−B_i films upon anodization that correlate to a dramatic enhancement in catalytic activity for O_2 evolution. By analogy of Ni−B_i to NiOOH, the results for Ni−B_i suggest that active sites of γ-NiOOH may be *intrinsically* more active toward the OER than those of β-NiOOH. In particular, the vast majority of studies of alkaline water oxidation mediated by nickel oxides have been conducted with nickel metal anodes[19,26,52−56] upon which an oxide coating is formed via electrochemical polarization. Since the surface oxide coating may grow substantially (up to 1.4 μm) during O_2 evolution,[19,52] the charge transport properties of the compact oxide layer are invariably convoluted with the kinetics of the OER at surface-exposed active sites.[16,57−59] Indeed, gradual deactivation of nickel anodes over time during alkaline OER, particularly when held at high overpotentials ($\eta \sim 600$ mV), has long been assigned to the formation of catalytically inert Ni(IV) centers within the surface oxide, leading to the contention that the all-Ni(III) phase, β-NiOOH, is the most catalytically active nickel anode material for mediating the OER.[19,26,52] In line with our observation for Ni−B_i, we propose the converse: that a predominantly Ni(IV) population, such as that found in the more highly oxidized γ-NiOOH-like structure, is paramount to high O_2 evolution activity. In our systems, Ni−B_i films are formed from solution precursors onto electrically conductive, oxidatively robust substrates, excluding interference from electron transport limitations, thus permitting isolation of the requirements for intrinsically efficient active-site turnover. To this end, the results reported herein stand at odds with prevailing dogma concerning nickel oxide-based O_2 evolution in alkaline media.

ASSOCIATED CONTENT

Supporting Information

Additional text, seven figures, and three tables with details on EXAFS curve fitting, estimation of film thickness, additional electrochemical traces, supplementary EXAFS spectra, structural models, and EXAFS fitting tables. This material is available free of charge via the Internet at http://pubs.acs.org.

AUTHOR INFORMATION

Corresponding Author

vkyachandra@lbl.gov; nocera@mit.edu

Notes

The authors declare no competing financial interest.

ACKNOWLEDGMENTS

We thank Dr. Jan Kern for help with collection of data. We are indebted to M. Dincă and D. Freedman for many helpful discussions. D.K.B. was supported by an MIT Energy Initiative predoctoral fellowship. Y.S. was supported by a National Science Foundation predoctoral fellowship. J.Y. and V.K.Y were supported by the Director, Office of Science, Office of Basic Energy Sciences (OBES), Division of Chemical Sciences, Geosciences, and Biosciences of the Department of Energy (DOE) under Contract DE-AC02-05CH11231. B.L.K. was also supported by the Helios Solar Energy Research Center, funded by OBES, DOE. Synchrotron facilities were provided by the Stanford Synchrotron Radiation Laboratory (SSRL) and the Advanced Light Source (ALS). The above centers and programs were supported by the OBES, DOE. The SSRL Biomedical Technology program is supported by the National Institute of Health (NIH), the National Center for Research Resources, and the DOE Office of Biological and Environmental Research. Part of this work was funded by DE-AC02-05CH11231. D.G.N. is indebted to joint support of this research from the DOE Catalysis and Solar Photochemistry programs.

REFERENCES

(1) Nocera, D. G. *Inorg. Chem.* **2009**, *48*, 10001−10017.
(2) Lewis, N. S.; Nocera, D. G. *Proc. Natl. Acad. Sci. U.S.A.* **2006**, *103*, 15729−15735.
(3) Abbott, D. *Proc. IEEE* **2010**, *98*, 42−66.
(4) Cook, T. R.; Dogutan, D. K.; Reece, S. Y.; Surendranath, Y.; Teets, T. S.; Nocera, D. G. *Chem. Rev.* **2010**, *110*, 6474−6502.
(5) Barber, J. *Chem. Soc. Rev.* **2009**, *38*, 185−196.
(6) Cukier, R. I.; Nocera, D. G. *Annu. Rev. Phys. Chem.* **1998**, *49*, 337−369.
(7) Huynh, M. H. V.; Meyer, T. J. *Chem. Rev.* **2007**, *107*, 5004−5064.
(8) Hammes-Schiffer, S. *Acc. Chem. Res.* **2009**, *42*, 1881−1889.
(9) Eisenberg, R.; Gray, H. B. *Inorg. Chem.* **2008**, *47*, 1697−1699.
(10) Siegbahn, P. E. M. *J. Am. Chem. Soc.* **2009**, *131*, 18238−18239.
(11) Concepcion, J. J.; Jurss, J. W.; Brennaman, M. K.; Hoertz, P. G.; Patrocinio, A. O. T.; Murakami Iha, N. Y.; Templeton, J. L.; Meyer, T. J. *Acc. Chem. Res.* **2009**, *42*, 1954−1965.
(12) Betley, T. A.; Wu, Q.; Van Voorhis, T.; Nocera, D. G. *Inorg. Chem.* **2008**, *47*, 1849−1861.
(13) Betley, T. A.; Surendranath, Y.; Childress, M. V.; Alliger, G. E.; Fu, R.; Cummins, C. C.; Nocera, D. G. *Philos. Trans. R. Soc. B* **2008**, *363*, 1293−1303.
(14) Dempsey, J. L.; Esswein, A. J.; Manke, D. R.; Rosenthal, J.; Soper, J. D.; Nocera, D. G. *Inorg. Chem.* **2005**, *44*, 6879−6892.

(15) Chang, C. J.; Chang, M. C. Y.; Damrauer, N. H.; Nocera, D. G. *Biophys. Biochim. Acta* **2004**, *1655*, 13−28.
(16) Surendranath, Y.; Nocera, D. G. *Prog. Inorg. Chem.* **2011**, *57*, 505−560.
(17) Tarasevich, M. R.; Efremov, B. N. In *Electrodes of Conductive Metal Oxides, Part A*; Trasatti, S., Ed.; Elsevier: Amsterdam, 1980; Chapt. 5.
(18) Trasatti, S. In *Electrochemistry of Novel Materials*; Lipkowski, J., Ross, P. N., Eds.; VCH: New York, 1994; Chapt. 5.
(19) Kinoshita, K. *Electrochemical Oxygen Technology*; Wiley−Interscience: New York, 1992; Chapt 2.
(20) McBreen, J. In *Handbook of Battery Materials*; Besenhard, J. O., Ed.; Wiley−VCH: Cambridge, U.K., 1999; pp 135−151.
(21) Pandya, K. I.; Hoffman, R. W.; McBreen, J.; O'Grady, W. E. *J. Electrochem. Soc.* **1990**, *137*, 383−388.
(22) Pandya, K. I.; O'Grady, W. E.; Corrigan, D. A.; McBreen, J.; Hoffman, R. W. *J. Phys. Chem.* **1990**, *94*, 21−26.
(23) Hu, Y.; Bae, I. T.; Mo, Y.; Antonio, M. R.; Scherson, D. A. *Can. J. Chem.* **1997**, *75*, 1721−1729.
(24) Mansour, A. N.; Melendres, C. A.; Wong, J. *J. Electrochem. Soc.* **1998**, *145*, 1121−1125.
(25) Mansour, A. N.; McBreen, J.; Melendres, C. A. *J. Electrochem. Soc.* **1999**, *146*, 2799−2809.
(26) Lyons, M. E. G.; Brandon, M. P. *Int. J. Electrochem. Sci.* **2008**, *3*, 1386−1424.
(27) Somorjai, G. A. *Introduction to Surface Chemistry & Catalysis*; Wiley: New York, 1994.
(28) Thomas, J. M.; Thomas, W. J. *Principles and Practice of Heterogeneous Catalysis*; VCH: Weinheim, Germany, 1997.
(29) Zambelli, T.; Wintterlin, J.; Trost, J.; Ertl, G. *Science* **1996**, *273*, 1688−1690.
(30) Jaramillo, T. F.; Jorgensen, K. P.; Bonde, J.; Nielsen, J. H.; Horch, S.; Chorkendorff, I. *Science* **2007**, *317*, 100−102.
(31) Kanan, M. W.; Yano, J.; Surendranath, Y.; Dincă, M.; Yachandra, V. K.; Nocera, D. G. *J. Am. Chem. Soc.* **2010**, *132*, 13692−13701.
(32) Dau, H.; Limberg, C.; Reier, T.; Risch, M.; Roggan, S.; Strasser, P. *ChemCatChem* **2010**, *2*, 724−761.
(33) Risch, M.; Klingan, K.; Heidkamp, J.; Ehrenberg, D.; Chernev, P.; Zaharieva, I.; Dau, H. *Chem. Commun.* **2011**, *47*, 11912−11914.
(34) Kanan, M. W.; Nocera, D. G. *Science* **2008**, *321*, 1072−1075.
(35) Surendranath, Y.; Dincă, M.; Nocera, D. G. *J. Am. Chem. Soc.* **2009**, *131*, 2615−2620.
(36) Lutterman, D. A.; Surendranath, Y.; Nocera, D. G. *J. Am. Chem. Soc.* **2009**, *131*, 3838−3839.
(37) Dincă, M.; Surendranath, Y.; Nocera, D. G. *Proc. Natl. Acad. Sci. U.S.A.* **2010**, *107*, 10337−10341.
(38) Esswein, A. J.; Surendranath, Y.; Reece, S. R.; Nocera, D. G. *Energy Environ. Sci.* **2011**, *4*, 499−504.
(39) Pijpers, J. J. H.; Winkler, M. T.; Surendranath, Y.; Buonassisi, T.; Nocera, D. G. *Proc. Natl. Acad. Sci. U.S.A.* **2011**, *108*, 10056−10061.
(40) Young, E. R.; Costi, R.; Nocera, D. G.; Bulović, V. *Energy Environ. Sci.* **2011**, *4*, 2058−2061.
(41) Reece, S. Y.; Hamel, J. A.; Sung, K.; Jarvi, T. D.; Esswein, A. J.; Pijpers, J. J. H.; Nocera, D. G. *Science* **2011**, *334*, 645−648.
(42) Nocera, D. G. *Acc. Chem. Res.* **2012**, DOI: 10.1021/ar2004013.
(43) Surendranath, Y.; Kanan, M. W.; Nocera, D. G. *J. Am. Chem. Soc.* **2010**, *132*, 16501−16509.
(44) Yang, X.; Takada, K.; Itose, M.; Ebina, Y.; Ma, R.; Fukuda, K.; Sasaki, T. *Chem. Mater.* **2008**, *20*, 479−485.
(45) Newville, M. *J. Synchrotron Radiat.* **2001**, *8*, 322−324.
(46) Rehr, J. J.; Albers, R. C. *Rev. Mod. Phys.* **2000**, *72*, 621−654.
(47) Bianconi, A. In *X-ray Absorption: Principles, Applications, Techniques of EXAFS, SEXAFS and XANES*; Koningsberger, D. C., Prins, R., Eds.; Wiley: New York, 1988; pp 573−662.
(48) Bartl, H.; Bode, H.; Sterr, G.; Witte, J. *Electrochim. Acta* **1971**, *16*, 615−621.
(49) Dyer, L. D.; Borie, B. S.; Smith, G. P. *J. Am. Chem. Soc.* **1954**, *76*, 1499−1503.
(50) Demourgues, A.; Gautier, L.; Chadwick, A. V.; Delmas, C. *Nucl. Instrum. Methods B* **1997**, *133*, 39−44.
(51) Oliva, P.; Leonardi, J.; Laurent, J. F. *J. Power Sources* **1982**, *8*, 229−255.
(52) Lu, P. W. T.; Srinivasan, S. *J. Electrochem. Soc.* **1978**, *125*, 1416−1422.
(53) Conway, B. E.; Liu, T. *J. Chem. Soc., Faraday Trans. 1* **1987**, *83*, 1063−1079.
(54) Conway, B. E.; Liu, T. C. *Mater. Chem. Phys.* **1989**, *22*, 163−182.
(55) Lyons, M. E. G.; Brandon, M. P. *Int. J. Electrochem. Sci.* **2008**, *3*, 1386−1424.
(56) Kinoshita, K. *Electrochemical Oxygen Technology*; Wiley−Interscience: New York, 1992; Chapt. 2.
(57) MacDonald, J. J.; Conway, B. E. *Proc R. Soc. London* **1962**, *269*, 419−440.
(58) Damjanovic, A; Jovanovic, B. *J. Electrochem. Soc.* **1976**, *123*, 374−381.
(59) Lyons, M. E. G.; Brandon, M. P. *Int. J. Electrochem. Sci.* **2008**, *3*, 1425−1462.